Light Scattering by Hexagonal Ice Crystals

RICH F. COLEMAN AND KUO-NAN LIOU

Department of Meteorology, University of Utah, Salt Lake City 84112

(Manuscript received 10 November 1980, in final form 25 February 1981)

ABSTRACT

A complete and traceable geometric ray-tracing solution for finite hexagonal columns and plates arbitrarily oriented in space has been developed by means of analytic geometry. In addition, an analytic expression for the cross-sectional area for arbitrarily oriented hexagons also has been derived based on which Fraunhofer diffraction and extinction and scattering cross sections in the limit of geometric optics can be computed exactly. The program involving geometrical reflection and refraction and Fraunhofer diffraction was used to compute the scattered intensities corresponding to two components of polarization for randomly oriented columns and plates in a horizontal plane and three-dimensional space. The scattered intensities were subsequently normalized to yield the nondimensional phase function commonly used in radiative transfer analyses. Numerical computations have been performed to study the effects of size, shape, orientation, and absorption on the scattering phase function and linear polarization. We show that the scattering phase functions for columns and plates, having approximately the same value, are quite similar except columns have a broader 22° halo pattern. The polarization patterns for these two shapes as well as for spheres and circular cylinders, however, are distinctly different, especially between 30 and 60° and between 130 and 140° scattering angles. We also show that hexagonal columns and plates randomly oriented in a horizontal plane do not generate a full scattering pattern of significant magnitude for an obliquely incident beam, and that the scattering patterns vary significantly with the oblique angle of the incident beam. At the 10.6 μm infrared wavelength, because of the strong absorption of ice, the scattering pattern is basically attributed to diffraction and external reflection but with a noticeable 7° halo maximum due to two refractions. Comparisons with experimental results for plates having a mode radius of 20 μm reveal a general agreement in regions from about 30–160° scattering angles.

1. Introduction

The angular scattering and polarization behaviors and the extinction property of ice crystals are fundamentally important to the development of remote sounding techniques for the inference of cloud compositions. They are also closely relevant to the radiative budget and hence the climate and climatic changes of the earth-atmosphere system. The determination of polarized light scattered by ice crystals is made very difficult because of their basic nonspherical structure and the consequent problem of orientation. Recognizing the importance for and the difficulty involved in the physical determination of the scattered radiation by nonspherical ice crystals, we have initiated and developed an experimental program at the University of Utah to investigate the angular scattering and polarization characteristics of ice crystals generated in the cold chamber utilizing a polarized He-Ne laser beam. Experimental results have been reported by Liou *et al.* (1976) and Sassen and Liou (1979a,b) in papers published in this journal.

However, ice crystals generated in the cold chamber have been limited to small sizes with a mode radius which normally is ≤ 10 μm and do not resemble the naturally occurring crystals in the atmosphere. Moreover, experimental findings generally do not provide adequate physical reasons for the understanding of scattering features produced by ice crystals. Such an understanding is imperative to the development of the cloud-sounding technique and to the evaluation of radiative transfer in planetary atmospheres. It is quite apparent that appropriate theoretical analyses need to be performed in addition to reliable experimental measurements to understand completely the scattering and polarization characteristics of nonspherical ice crystals.

On the theoretical side, Liou (1972) for the first time proposed and developed ice cloud models in conjunction with scattering computations based on the assumption that ice clouds are composed of long circular cylinders. However, ice crystals occurring in the earth's atmosphere generally preserve the basic hexagonal structure which will generate no rainbow features caused by curvature effects, but will produce significant scattering maxima known as halos. Humphreys (1929) in his book outlined procedures to compute the position of the maximum intensity scattered from hexagonal crystals. Recently, Greenler *et al.* (1977) developed a compre-

0022-4928/81/061260-12$07.00

hensive code to locate positions of halos and other complex arcs produced by ice crystals. However, the angular scattering pattern was not evaluated until the work published by Jacobowitz (1971). In his paper, Jacobowitz utilized a geometrical ray-tracing program for an infinitely long column and showed a number of illustrating scattering diagrams for various orientations. Jacobowitz did not give analytic ray-tracing procedures in his program. More recently, Wendling *et al.* (1979) carried out a more comprehensive scattering analysis for finite hexagons, also based on the ray-tracing principle. Their method is a statistical one and does not give traceable procedures in such a manner that scattering events due to individual reflection and/or refraction can be accounted for. Both Jacobowitz and Wendling *et al.* considered no effect of polarization nor absorption within the hexagonal crystal. Both assumed a rectangular aperture for diffraction calculations which leads to errors when the incident beam is oriented from normal. Moreover, except for scattering phase functions, scattering and extinction cross sections for oriented hexagonal crystals have not been derived in the context of geometric ray optics.

In this paper, in parallel to our earlier and present experimental and theoretical programs for light scattering and cloud physics studies, we have developed a geometric-ray tracing program for finite hexagonal columns and plates randomly oriented in two- or three-dimensional space by means of analytic geometry involving a hexagon. The program also includes exact expressions for diffraction and extinction and scattering cross sections for an arbitrarily oriented hexagon. Traceable ray-tracing procedures and basic equations associated with geometric optics and diffraction are outlined and described. Computations have been carried out to investigate the effects of shape, size, orientation and absorption on the scattering phase function and linear polarization. Highlights of the computational results are presented and physically discussed.

2. Fundamental ray-tracing program for hexagonal crystals

a. Geometrical optics

In this section we briefly describe the procedures for computing the scattered intensity for a finite number of rays undergoing external reflection, two refractions and internal reflections. We use a Cartesian coordinate system with origin fixed at the center of the crystal. The Z axis passes through the center of the top and bottom faces and the $X-Y$ plane cuts the crystal, giving a regular hexagon at any value of Z. Fig. 1 shows the X, Y and Z axes as well as two orientation angles associated with a typical ray. The angle θ is the angle between the $X-Y$ plane and the rays and ϕ is the azimuthal angle.

As shown in Fig. 1, the angle τ is the angle between the ray and the surface normal. In terms of the angles ϕ and θ, the angle τ is simply given by $\cos\tau = \cos\phi \times \cos\theta$. Using trigonometric relations between the angles depicted in Fig. 1, it can be shown that the conventional Snell's law may be expressed in terms of the azimuthal angle ϕ and the elevation angle θ as follows:

$$\left.\begin{aligned} \sin\theta &= m_r \sin\theta' \\ \sin\phi &= m_r' \sin\phi' \\ m_r' &= \frac{m_r \cos\theta'}{\cos\theta} \end{aligned}\right\}, \tag{1}$$

where θ' and ϕ' are angles corresponding to the refracted ray. The separation of the Snell's refraction law into two components allows the trace of rays separately on the $X-Y$ plane of the hexagon and along the Z axis.

In order to calculate reflected and transmitted energy, as well as linear polarization, we make use of the general Fresnel coefficients involving internal absorption. Let the real and imaginary parts of the complex index of refraction be denoted as m_r and m_i, respectively, then the reflection coefficients are given by (Born and Wolf, 1975)

$$\left.\begin{aligned} R_1(\tau) &= \frac{(\cos\tau - u)^2 + v^2}{(\cos\tau + u)^2 + v^2} \\ R_2(\tau) &= \frac{[(m_r^2 - m_i^2)\cos\tau - u]^2 + (2m_r m_i \cos\tau - v)^2}{[(m_r^2 - m_i^2)\cos\tau + u]^2 + 2m_r m_i \cos\tau + v)^2} \end{aligned}\right\}, \tag{2}$$

where τ is the angle between the surface normal and the ray as mentioned previously, and

$$\left.\begin{aligned} u^2 &= \tfrac{1}{2}\{m_r^2 - m_i^2 - \sin^2\tau + [(m_r^2 - m_i^2 - \sin^2\tau)^2 + 4m_r^2 m_i^2]^{1/2}\} \\ v^2 &= \tfrac{1}{2}\{-(m_r^2 - m_i^2 - \sin^2\tau) + [(m_r^2 - m_i^2 - \sin^2\tau)^2 + 4m_r^2 m_i^2]^{1/2}\} \end{aligned}\right\}. \tag{3}$$

The corresponding transmission coefficients are defined as

$$\left.\begin{aligned} T_1 &= 1 - R_1 \\ T_2 &= 1 - R_2 \end{aligned}\right\}. \tag{4}$$

Having the Snell's law and Fresnel coefficients defined, we now require the evaluation of the incident and refracted angles for each reflection/refrac-

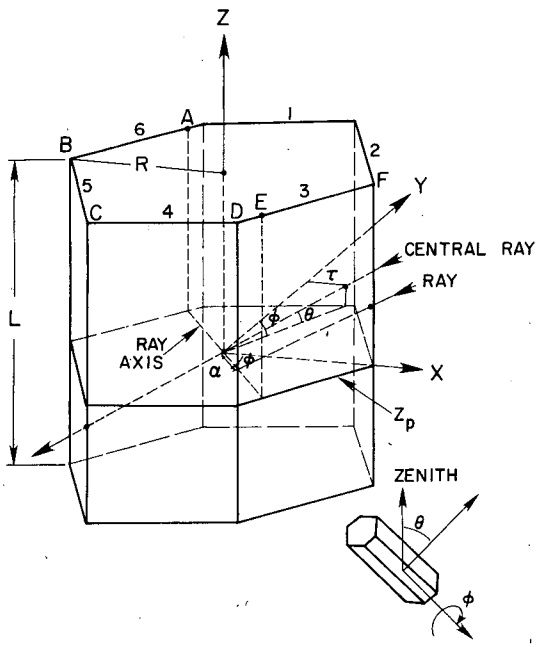

FIG. 1. General geometry of light rays incident on hexagonal crystals.

tion event which will involve the basic geometric properties of hexagonal crystals. For the sake of brevity, detailed geometric equations associated with the ray-tracing program will not be presented here. But rather we shall describe the basic procedures employed in the computation.

First, we note that the length of a side of a hexagon is the same as the radius of the circumscribed circle R and that there are eight faces involved for a hexagon. In addition, we see that the angle between adjacent sides is 120°, while the angle between surface normals for adjacent sides is 60°. Thus, in the $X-Y$ plane if one side of the hexagon is perpendicular to and intersects the positive Y axis (labeled face 1 in Fig. 1), then the slopes of the remaining faces (numbered 2–6 in the clockwise direction) will be $-\tan 60°$, $\tan 60°$, $\tan 0°$, $-\tan 60°$ and $\tan 60°$, respectively. Their Y intercepts are $R\cos 30°$ for 1 and 4, $R\tan 60°$ for 2 and 6, and $-R\tan 60°$ for 3 and 5.

Next, we need to describe the crystal and the position and orientation of all the rays in the light ray volume with respect to the crystal. In Fig. 1 a typical hexagonal cylinder is shown with one ray plane incident on it. Two variables are associated with the crystal size and shape. They are the radius R and the length L. Moreover, we define two orientation angles which are denoted as θ and ϕ. The elevation angle θ is 90° minus the angle between the Z axis and the light ray. The azimuthal angle ϕ is the measure of the rotation of the light ray volume about the Z axis. In each ray plane, a line is drawn perpendicular to the light rays which pass through the Z axis. This is the ray axis shown in Fig. 1. The number of rays along this line is denoted as NR. The light ray in each ray plane which intersects the Z axis is the central ray. One central ray is assumed to have $Z = 0$. Finally, we need a variable to define the ray plane spacing so that incident rays can be properly accounted for along the vertical direction.

Once the relative position of the hexagon with respect to a volume of incident rays has been defined, the first set of refracted angles in terms of the incident angles mapped on the principle plane ($X-Y$ plane) and the elevation angle may be obtained through the Snell's law. On the basis of analytic geometry, we determine the coordinates and direction cosines of each entering ray which may be incident on the top or side surfaces. Since both the Fresnel coefficients and Snell's law depend on angles relative to the surface normal, it is necessary to determine these relative angles for the eight faces from the azimuthal and elevation angles ϕ and θ. We then trace the ray through the crystal and find the face and the point that the ray will intercept, utilizing the known coordinates of the entry point, the angle between the incident and refracted rays, and the slope of the refracted ray. Subsequently, the coordinates for the point on a specific crystal surface (either top or side) as well as the internal path length, which is required to account for internal absorption, may be geometrically determined. Moreover, the relative azimuthal and elevation angles at the exit point may be obtained geometrically from those at the entry point. Three cases involving the determination of the relative elevation angle are shown in Fig. 2 along with the general ray-tracing geometry for a hexagon. Thus, the scattered energy due to two refractions may be derived and the scattering angle is to be determined from the direction cosines for the entry and exit rays. Note that the externally reflected angles are exactly the same as the incident angles and therefore the computation for the scattered energy is relatively simple and straightforward. Using the preceding procedures, we may find the necessary angles, slopes and direction cosines to determine the position of the one internally reflected ray and the crystal face which it will intercept. Fresnel coefficients may be computed through the use of the Snell's law at each intercept and the reflected and transmitted energy and the associated scattering angle and absorption path length evaluated thereafter.

In order to obtain the conventional scattering phase function and single-scattering parameters, it is desirable to define the transmitted and reflected intensities. In the context of geometric optics, we may describe the number of rays per unit area normal to their direction of travel and assume that the energy of each ray is evenly distributed over this unit area. We then assume that the ray is located somewhere in a small but finite solid angle $d\Omega$ about the normal to the unit area da and that this ray

carries one unit of energy across the unit area in unit time (i.e., differential flux df). Hence, the intensity of the ray is defined as $I = df/(da d\Omega)$. If the surface of interest is oriented at some angle τ with respect to the direction of travel of the rays then the intensity becomes $I = df/(\cos\tau da d\Omega)$. On the basis of the geometrical consideration for a smooth surface, the intensity reflected from such a surface for each polarization component is simply

$$I^r_{1,2} = R_{1,2}(\tau) I^i_{1,2}. \tag{5}$$

To obtain the transmitted intensity I^t, we utilize the flux conservation principle involving an unit area and we find for either polarization component

$$I^i \cos\tau_i da d\Omega_i = I^r \cos\tau_i da d\Omega_i + I^t \cos\tau_t da d\Omega_t, \tag{6}$$

where τ_i and τ_t are the incident and transmitted angles, respectively, and $d\Omega_i$ and $d\Omega_t$ are the differential elements of solid angle about the incident and transmitted rays, respectively. Using the definition of solid angle and Snell's law, it can be shown that

$$I^t_{1,2} = m_r^2 I^i_{1,2}[1 - R_{1,2}(\tau_i)]. \tag{7}$$

In writing this expression, it is assumed that the surrounding medium has an index of refraction of unity. The relation between the incident and the reflected and transmitted intensities makes it possible to determine the scattered intensity from a large number of rays.

Finally, the total scattered intensity from all incident rays due to geometrical reflection and refraction may be written in the form

$$I^{(p)}_{1,2}(\Theta) = \exp(-2km_i l_p) \begin{cases} \sum_j R_{1,2}(\tau_{1j}) I^i_{1,2}, & p = 0 \\ \sum_j [1 - R_{1,2}(\tau_{1j})][1 - R_{1,2}(\tau_{2j})] I^i_{1,2}, & p = 1 \\ \sum_j [1 - R_{1,2}(\tau_{1j})][1 - R_{1,2}(\tau_{(p+1)j})] \prod_{n=2}^{p} R_{1,2}(\tau_{nj}) I^i_{1,2}, & p \geq 2 \end{cases} \tag{8}$$

where the index p denotes the contribution of the scattered energy: $p = 0$, external reflection; $p = 1$, two refractions; and $p \geq 2$, internal reflection. l_p is the ray path length in the crystal and $l_p = 0$ when $p = 0$, k the wave number, and j the index for the entry rays. At this point, we have described the required geometric ray tracing procedures for a general orientation position.

b. *Fraunhofer diffraction*

To compute the diffraction component of the scattered intensity, we need to derive the geometric cross-sectional area for any arbitrary orientation. The cross-sectional area as seen when the crystal is observed from an orientation with angles of θ and ϕ is determined by projecting the outlines of the crystal onto a plane normal to the direction of observation. After a number of tedius geometrical analyses, the end result is given by

$$D(R, L, \theta, \phi) = 3R(R \sin\tfrac{1}{3}\pi \sin\theta + \tfrac{1}{3}L \cos\phi \cos\theta). \tag{9}$$

This area represents the diffraction aperture for rays oriented at θ and ϕ with respect to a crystal with length L and radius R. In making the projection to determine the area, the coordinates of the sides of the aperture are also determined and may be used as the integration limits for the Fraunhofer integral described below. Also, note that the total geometric area is simply given by $G(R, L) = 6R(L + R \times \sin\pi/3)$.

We apply the Kirchhoff's integral, in the Fraunhofer limit, over the cross-sectional aperture to determine the diffraction pattern at a distant observation point as shown in Fig. 3. The electric field at $\mathbf{r}$ is given by (Schwartz, 1972)

$$E(\mathbf{r}) = \frac{-ikE_0}{2\pi} \int_D \frac{\exp(-ik|\mathbf{r} - \mathbf{r}'|)}{|\mathbf{r} - \mathbf{r}'|} da', \tag{10}$$

where $k = 2\pi/\lambda$, E_0 is the incident electric field, and D is the area of the aperture. In the Fraunhofer limit we have

$$|\mathbf{r} - \mathbf{r}'| \approx r - \frac{\mathbf{r}\cdot\mathbf{r}'}{r}. \tag{11}$$

Thus, we may write the integral as

$$E(\mathbf{r}) \approx \frac{-ikE_0 e^{ikr}}{2\pi r} \int_D \exp(ik\mathbf{r}\cdot\mathbf{r}'/r) da'. \tag{12}$$

Moreover, from Fig. 3 we see that the coordinates of the points $\mathbf{r}'$ and $\mathbf{r}$ are given by

$$\left.\begin{aligned} x' &= |r'| \cos\phi, & y' &= |r'| \sin\phi, \\ x &= |r| \sin\Theta \cos\Phi, & y &= |r| \sin\Theta \sin\Phi \end{aligned}\right\}. \tag{13}$$

If we let $k \sin\Theta = k'$ and $\cos\Phi = \mu$, Eq. (12) becomes

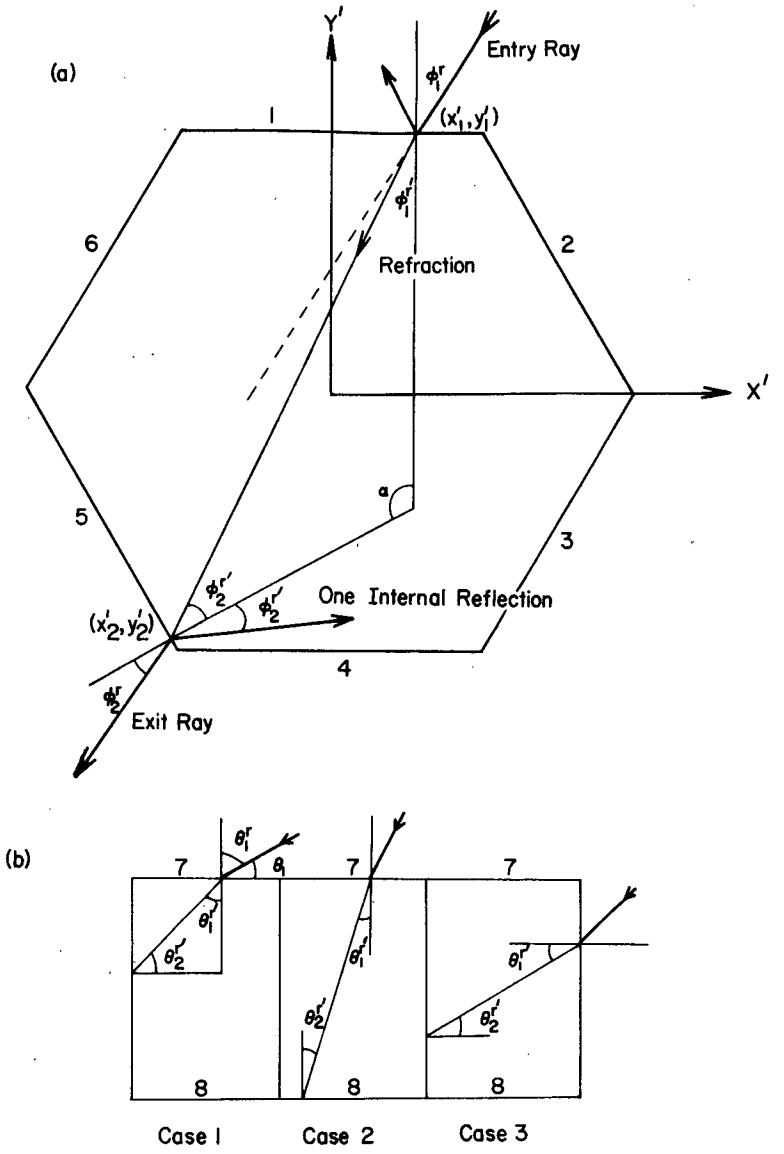

FIG. 2. Exit ray geometry including exit points and internal angles (see text for explanations).

$$E(\mathbf{r}) = \frac{-ikE_0}{\pi r} \times \int_D \exp\{ik'[\mu x' + (1-\mu^2)^{1/2}y']\}dy'dx'. \quad (14)$$

The intensity in terms of Θ and Φ may be expressed by

$$I(\Theta, \Phi) = I(\Theta, \mu) = \frac{cr^2}{8\pi}|E(\mathbf{r})|^2, \quad (15)$$

where c is the speed of light. We then integrate Eq. (14) over the aperture to obtain

$$|E|^2 = \frac{k^2E_0^2}{(\pi rk')^2(1-\mu^2)}\{[-\alpha_0 \sin\beta_0 + \alpha_1 \sin\beta_1 + \alpha_2 \sin\beta_2 + \alpha_3 \sin\beta_3 \cos\beta_4 + \alpha_4 b_1 \sin(\beta_3 + \beta_4) - \alpha_4 b_3 \sin(\beta_3 - \beta_4)]^2 + [-\alpha_1 \cos\beta_1 - \alpha_2 \cos\beta_2 + \alpha_3 \sin\beta_3 \sin\beta_4 - \alpha_4 b_1 \cos(\beta_3 + \beta_4) + \alpha_4 b_3 \cos(\beta_4 - \beta_3)]^2\}, \quad (16)$$

where

$$\alpha_0 = 2/k'\mu, \quad \beta_0 = k'\mu x_B',$$
$$\beta_1 = (\mu x_D' + \sqrt{1-\mu^2}y_D'),$$
$$\beta_2 = k'(\mu x_c' + \sqrt{1-\mu^2}y_c'),$$

$$\beta_3 = k'(\mu y_B' + a\sqrt{1-\mu^2}), \quad \beta_4 = k'b\sqrt{1-\mu^2},$$

$$\alpha_1 = (b_2 - b_1)\sqrt{1-\mu^2} \div [k'(\mu + b_1\sqrt{1-\mu^2})(\mu + b_2\sqrt{1-\mu^2})],$$

$$\alpha_2 = (b_3 - b_2)\sqrt{1-\mu^2} \div [k'(\mu + b_3\sqrt{1-\mu^2})(\mu + b_2\sqrt{1-\mu^2})],$$

$$\alpha_3 = 2\mu/[k'(\mu + b_1\sqrt{1-\mu^2})(\mu + b_3\sqrt{1-\mu^2})],$$

and $a = R\sin\phi$, $b = L\cos\theta/2$, $b_1 = \tan\pi/3\sin\theta$, $b_2 = \tan\phi\sin\theta$, $b_3 = -\tan(\pi/3 - \phi)\sin\theta$, and (x_B', y_B'), (x_c', y_c'), and (x_D', y_D') are the projected coordinates of the points B, C and D, respectively, shown in Fig. 1.

In order to determine the average value of the diffraction intensity at a given scattering angle Θ, we perform integration of $I(\Theta, \Phi)$ over all possible values of Φ to get

$$I(\Theta) = \frac{1}{2}\int_{-1}^{1} I(\Theta, \mu)d\mu = \frac{1}{2}\int_{-1}^{1} \frac{cr^2|E(\mathbf{r})|^2}{8\pi} d\mu. \quad (17)$$

This is the diffracted intensity at a particular crystal orientation.

c. *Phase function and extinction and scattering cross sections*

Using the definition of the scattered intensity for geometrical reflection and refraction and diffraction, we may now define the scattering phase function, which represents the probability of scattering into a given angle relative to the probability of scattering into that angle by an isotropic scatterer. We find the isotropically scattered intensity by summing all the scattered intensity and then multiplying by the fraction of the total solid angle concerned. For each polarization component, the phase function $P_{1,2}(\Theta)$ is the intensity scattered into Θ divided by the computed isotropically scattered intensity defined by

$$P_{1,2}(\Theta_i) = \frac{1}{2}\frac{4\pi}{2\pi\Delta\cos\Theta_i} \times \left[\frac{\sum_P I_{1,2}^{(P)}(\Theta_i)}{\sum_j \sum_P I_{1,2}^{(P)}(\Theta_{i,j})} + \frac{I^f(\Theta_i)}{\sum_j I^f(\Theta_{i,j})}\right], \quad (18)$$

where $I_{1,2}^{(P)}$ is the intensity for geometrical reflection and refraction and I^f is the diffracted intensity. From the scattering phase function, the linear polarization ratio may be defined and is given by

$$\mathrm{LP}(\Theta) = \frac{P_1(\Theta) - P_2(\Theta)}{P_1(\Theta) + P_2(\Theta)}. \quad (19)$$

Note that a brief but analogous discussion concerning ray tracing through a hexagon has also been presented by Liou (1980).

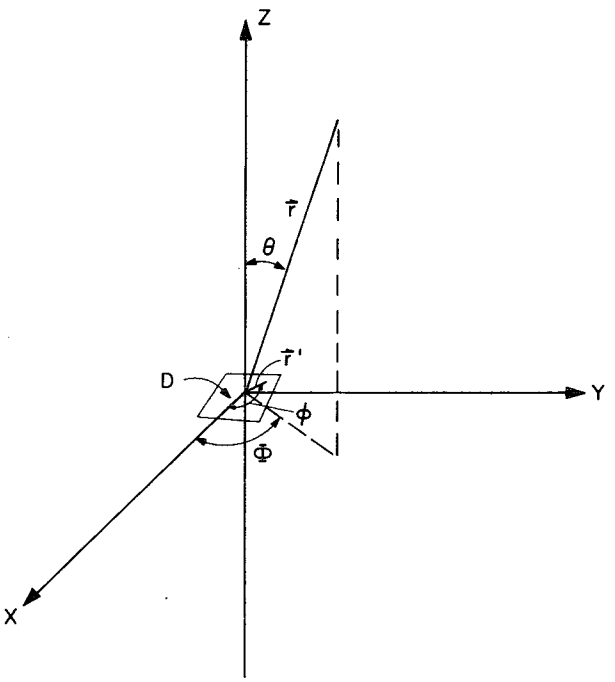

FIG. 3. Geometry for diffraction.

In addition, we wish to derive the extinction and scattering cross sections in the limit of geometric optics. Let the geometric cross-sectional area be D, and the diffracted, scattered, and absorbed flux be f_d, f_s and f_a, respectively. Thus, we have $f_d = f_s + f_a$. By definition, the incident flux density is given by the incident flux divided by D. Also, the incident flux is simply equal to either the diffracted flux or the sum of the refracted and absorbed flux. Thus, according to the optical theorem, the extinction cross section may be defined by

$$\sigma_e = \frac{f_d + f_s + f_a}{f_d/D} = 2D. \quad (20)$$

The scattering cross section is then given by

$$\sigma_s = \frac{f_d + f_s}{f_d/D} = D\left(1 + \frac{f_s}{f_d}\right). \quad (21)$$

It follows that the absorption cross section is

$$\sigma_a = \sigma_e - \sigma_s, \quad (22)$$

and the single-scattering albedo is

$$\tilde{\omega} = \frac{\sigma_s}{\sigma_e} = \frac{1}{2}\left(1 + \frac{f_s}{f_d}\right). \quad (23)$$

All the above analyses and discussions are concerned with crystals having a specific orientation. It should be noted that in order to obtain a full scattering pattern for a hexagonal crystal, it is necessary

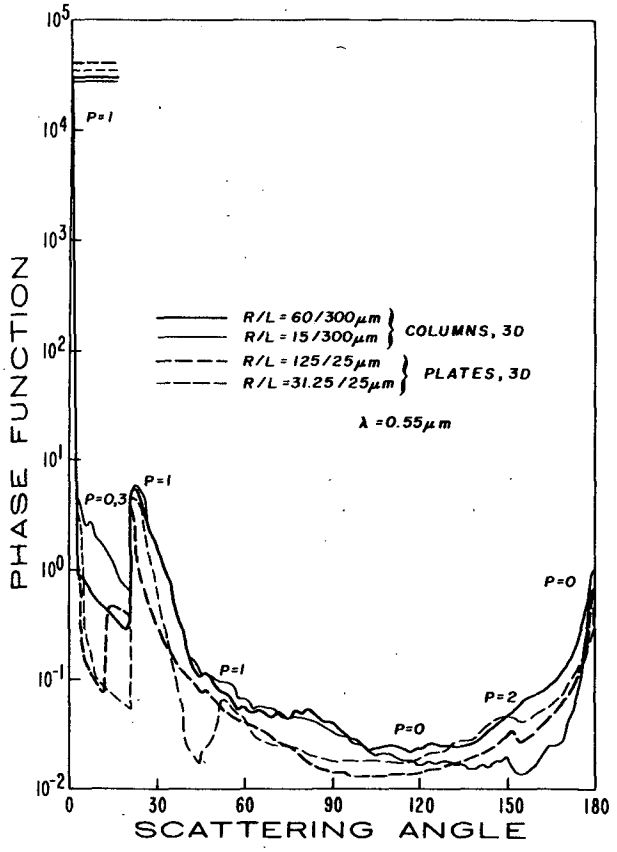

FIG. 4. Effects of size and shape on 3D (three-dimensional random orientation) phase functions.

to rotate the crystal about its central axis so that all crystal faces are exposed to the incoming light beam. The scattering phase function in this case is expressed in terms of the scattering angle Θ, the elevation angle θ, and the azimuthal angle ϕ (see Fig. 1). To obtain the scattering pattern for a sample of equal-sized crystals randomly oriented in a plane or in three-dimensional space, we are required to perform orientation integration. For random orientation in a plane such that all possible orientation positions for crystals are accounted for in that plane, we write (see, e.g., Liou, 1972)

$$\left.\begin{matrix} P(\Theta, \theta) \\ \sigma_{e,s}(\theta) \end{matrix}\right\} = \frac{2}{\pi} \int_{\theta}^{\pi/2} \left\{\begin{matrix} P(\Theta; \theta, \phi) \\ \sigma_{e,s}(\theta, \phi) \end{matrix}\right\} d\phi, \qquad (24)$$

where the azimuthal integration is done over the range of $(0, \pi/2)$ because of the symmetry of the hexagonal crystals. For three-dimensional random orientation, we find

$$\left.\begin{matrix} P(\Theta) \\ \sigma_{e,s} \end{matrix}\right\} = \frac{2}{\pi^2} \int_{0}^{\pi} \int_{0}^{\pi/2} \left\{\begin{matrix} P(\Theta; \theta, \phi) \\ \sigma_{e,s}(\theta, \phi) \end{matrix}\right\} d\phi d\theta, \qquad (25)$$

where, in principle, the range of integration for the elevation angle is from $(0, \pi)$. However, in numerical computations, we find the scattering pattern is symmetric in the intervals $(0, \pi/2)$ and $(\pi/2, \pi)$. Also, from the computational point of view, it is assumed that when any ray which is scattered into an angle within plus or minus half a degree of an integer degree it is considered to be scattered into that integer degree. Thus, if the scattering angle is 0.75°, it is assumed to be scattered at 1°. This has been done as an inherent averaging process. Moreover, after a number of numerical experimentations we find that accurate scattering patterns may be constructed by using an angular increment of 0.5 in both azimuthal and zenith directions for three-dimensional random orientation cases.

3. Results

In this section we present results of phase function, linear polarization and cross-section calculations. The calculations have been made for four representative crystals: a large column with $R = 60$ μm and $L = 300$ μm; a small column with $R = 15$ μm and $L = 300$ μm; a large plate with $R = 125$ μm and $L = 25$ μm; and a small plate with $R = 31.25$ μm and $L = 25$ μm. Wavelengths of 0.55 and 10.6 μm along with the refractive indices of 1.31 and $1.097 + 0.134i$, respectively, for ice are used in this study.

Fig. 4 shows the effects of size and shape on the scattering phase functions for randomly oriented columns and plates. Results for large and small columns are denoted by heavy and light solid lines, respectively, while results for large and small plates are represented by heavy and light dashed lines, respectively. The features normally associated with hexagonal ice crystals are immediately apparent for all four crystals. These include (i) the very strong forward scattering peak caused by diffraction and by two refractions ($p = 1$), (ii) the 22° halo, very sharp on the inner edge but diffuse on the outer, caused by two refractions ($p = 1$), (iii) the strong backward scattering caused mainly by specular reflection ($p = 0$) from the side and end faces, (iv) the 46° halo caused by two refractions ($p = 1$), and (v) the small peak between 150 and 159° caused by one internal reflection ($p = 2$). Except for small plates, the 46° halo is rather weak. The physical origin of these features will be discussed in the next section. Having noted the features common to all four crystals (and indeed common to all hexagonal cylinders), we wish to discuss the effects of size and shape on each of them.

In regard to the effects of shape, the major differences occur between 0 and 105° scattering angles. At the 0° scattering angle we see that plates are more efficient scatterers, which is directly attributable to the greater effect of the end faces on plates than on columns. Between 3 and 105° scattering

angles, however, the columns are more effective. This is due to the difference in relative importance of the 90° prism angle (between end and side faces) and the 60° prism angle (between side faces). The plates show more effects from the 90° prism angle than do the columns.

Two other shape effects need to be noted. These effects, however, are also partially related to size. The first is a small but distinct 8° halo revealed by the small column. This feature occurs in the crystal having the smallest R/L ratio, which resembles a needle, and represents the opposite extreme to the large plate, which is effectively two parallel scattering surfaces. The 8° halo appears to be a result of external ($p = 0$) and two internal ($p = 3$) reflections, with both internal reflections occurring on side faces. It only occurs at high elevation angles, restricting it to long narrow crystals. The second shape/size effect is the 46° halo. This halo is the path of minimum deviation for a 90° prism angle. Thus, we would expect it to be more predominant in the plate than the column. In spite of this, it is almost nonexistent in the large plate case. This is because the amount of light which is scattered by an end-side face combination is much smaller than that which is scattered by one or a combination of end faces for the large plate. In effect the 46° halo is swamped by the external reflection profile for the large plate crystal. The small plate, on the other hand, provides much greater opportunity for the end-side combination than do any of the other crystals, resulting in a very strong 46° halo.

Pure size effects, for a given crystal shape, are much more elusive than shape effects. They are most noticeable at 0 and 180°. In both shapes, the larger crystal has a larger value at 0° (larger diffraction aperture) and at 180° (greater surface area available for specular reflection). In addition, the feature around 150° tends to be more predominant for the smaller crystal in each shape.

Fig. 5 shows the orientation effect on the phase functions for crystals randomly oriented in a plane. We have plotted the phase function value as a function of both scattering (Θ) and elevation (θ) angle for the large column. The resulting surface presents a number of interesting aspects. First, we see that the value of the forward scattering increases slightly with increasing elevation angle, caused by the increasing effect of the end faces. Next, the specular reflection points, at each orientation, are given by $\Theta = |\pi - 2\theta|$ (specular reflection on the side faces with $\phi = 0$) and $\Theta = 2\theta$ (specular reflection on the end face at any ϕ). These points form two "cliffs" with one running from the point $(\Theta, \theta) = (\pi, 0)$ to the point $(\Theta, \theta) = (0, \pi/2)$ and one running from the point $(\Theta, \theta) = (0, 0)$ to the point $(\Theta, \theta) = (\pi, \pi/2)$. The cliff from (0, 0) to (104°, 60°) is swamped under the refraction "mountain," but is quite visible beyond this point. This third major feature is the halo mountain which has its highest point at (22°, 0) and progresses to the point (63°, 90°). The shift from $\Theta = 22°$ to $\Theta = 63°$ is a function of the increasing index of refraction as θ increases. The irregular isolated feature centered near (170°, 70°) is completely dependent on the presence of end faces and is caused by multiple internal reflections ($p > 1$).

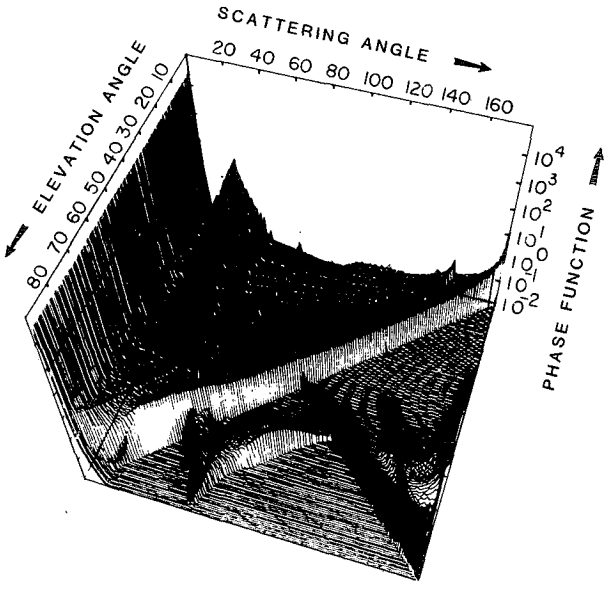

FIG. 5. Effects of orientation on 2D (random orientation in a plane) phase functions.

Fig. 6 illustrates the effects of wavelength on the phase functions for randomly oriented crystals. The heavy solid line is for the large column in the visible, while the light solid line is for the large column in the infrared. The heavy and light dashed lines are for the large plate in the visible and infrared, respectively. In both cases, we see that the infrared diffraction peaks are lower and broader, as expected. The 22 and 46° halos have shifted to 7 and 27°, respectively. Both shifts are due to the change in the real part of the index of refraction. Due to the small effect of the 60° prism angle on the large plate, the 7° halo lies in a well which is formed by the diffraction peak and the beginning of the external reflection profile at 15°. This shows very effectively the strong absorption which takes place at this wavelength. In fact, the entire profile, for both infrared cases, is an external reflection profile ($p = 0$), except for the 7 and 27° halos. The lower diffraction peak has the effect of broadening the backscattering peak and raising the entire profiles relative to the visible, except at the 22° halo. This of course does not represent higher energy values, only greater scattering probabilities in angles other than the forward direction. The plot of cross sections and albedo shows this more directly (see Fig. 11).

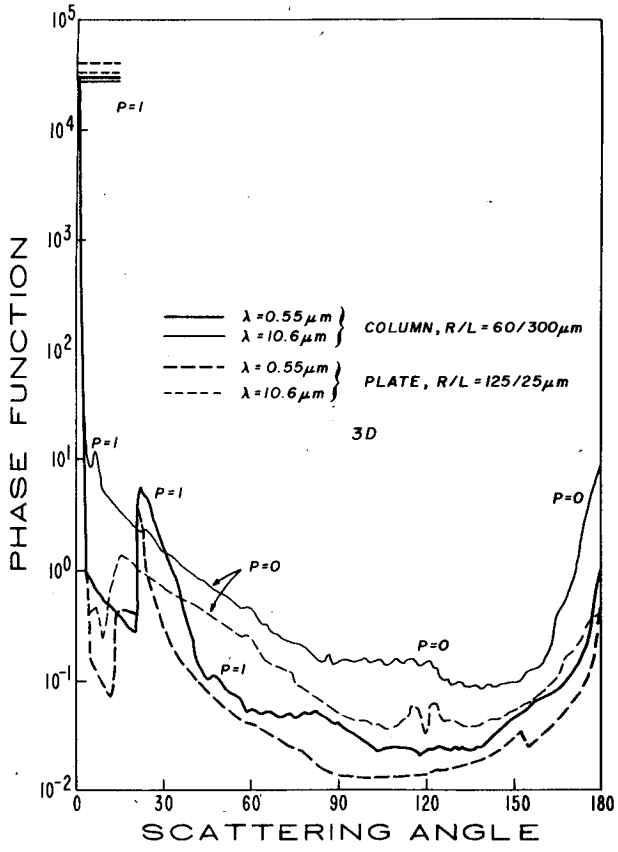

FIG. 6. Effects of wavelength on 3D phase functions.

Fig. 7 compares the scattering phase function for randomly oriented columns at $\lambda = 0.55$ μm obtained from the present study and from those of Jacobowitz (1971) and Wendling *et al.* (1979). As can be seen in the figure the major differences between the result of Jacobowitz and the result in the present study are the increased scattering in the region between 2 and 20° and between 160 and 180°. As noted previously these areas are regions where end effects are most predominant. Since Jacobowitz's calculations were made for infinitely long crystals ($L = \infty$) and did not take into account the end effects, the differences between the two curves are physically understood. The result of Wendling *et al.* shows very close correspondence to the present study so far as all of the scattering features on the curve are concerned, but the difference in energy is quite significant. It is believed that the difference is in part due to the different ratio R/L used (1/5 for the present study and 1/10 for the Wendling's study) and partly due to the fact that Wendling *et al.* averaged their result over 2° increments, while in the present study averaging is made over 1° increments in the scattering angle.

Fig. 8 presents a phase function comparison for randomly oriented large plates (dashed line) and columns (solid line) and for spheres (Liou and Hansen, 1971). The spheres used have a mode radius of 100 μm. The previously noted features for the plate and column contrast sharply with the sphere in two scattering regions. Between 3 and 36° scattering angles the sphere shows a smooth decrease, while the strong near forward and halo scattering expected from a hexagonal crystal shows for both columns and plates. At 132 and 140° scattering angles the secondary and primary rainbows are seen for spheres, while no corresponding feature is exhibited by plates and columns. It should be noted that the 22° halo, especially for the column, is nearly an order of magnitude larger than the rainbow. This is entirely due to the fact that the halo is caused by two refractions ($p = 1$), while the rainbow (in geometric optics) is generated by one internal reflection ($p = 2$). Energy losses by internal reflections are much greater than by two refractions.

Fig. 9 illustrates a comparison of the linear polarization produced by randomly oriented large plates (dashed line), randomly oriented large columns

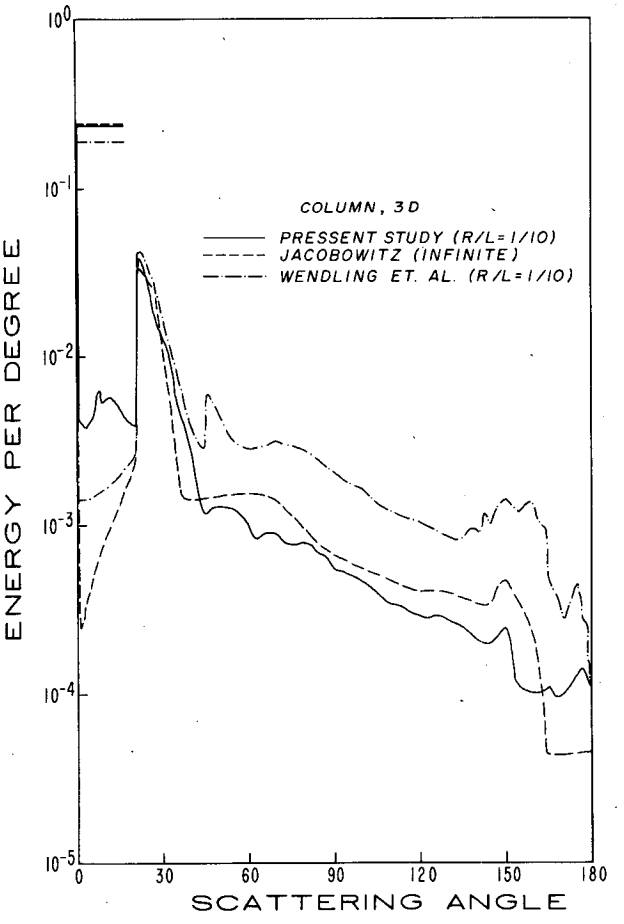

FIG. 7. Comparison of scattered energy for randomly oriented columns from the present study, Jacobowitz (1971) and Wendling *et al.* (1979).

(solid line), spheres (dash-dot line), and randomly oriented long circular cylinder (dotted line). Calculations for spheres were made using geometric optics (Liou and Hansen, 1971) and therefore polarization characteristics are independent of the size of the sphere. The cylinder results are taken from Liou (1972) in which the ratio for the cylinder is $R/L = 10\ \mu m/\infty$. The polarization for plates and columns has the expected negative values in the halo region, but is everywhere else positive. The predominance of end effects in plates versus columns is shown very clearly in the region from 22 to 105° scattering angles. The much broader negative halo region, the greater drop at 46° and the broad dip between 57 and 99° scattering angles for columns all demonstrate the greater influence of two refractions for columns than plates. In contrast to hexagonal crystals, spheres and circular cylinders both depict a negative polarization in the region from 30 to 60° scattering angles and very sharp peaks near the two cloud bow regions. In addition, the polarization curve for circular cylinders becomes strongly negative in the region from 160 to 174° scattering angles.

In Fig. 10 we present a comparison of phase functions for randomly oriented columns (solid line) and plates (dashed line) and experimental data for small plates in the region from 10 to 175° scattering angles (Sassen and Liou, 1979a). The modal diameter for plates is $d_m = 20\ \mu m$. The agreement for theory and experiment, even with these small plates, appears to be generally good except that no halo is observed in the experimental data. Note that the scattering phase functions for spheres will have rainbow and glory features and much lower side scattering and therefore they cannot fit the experimental data properly.

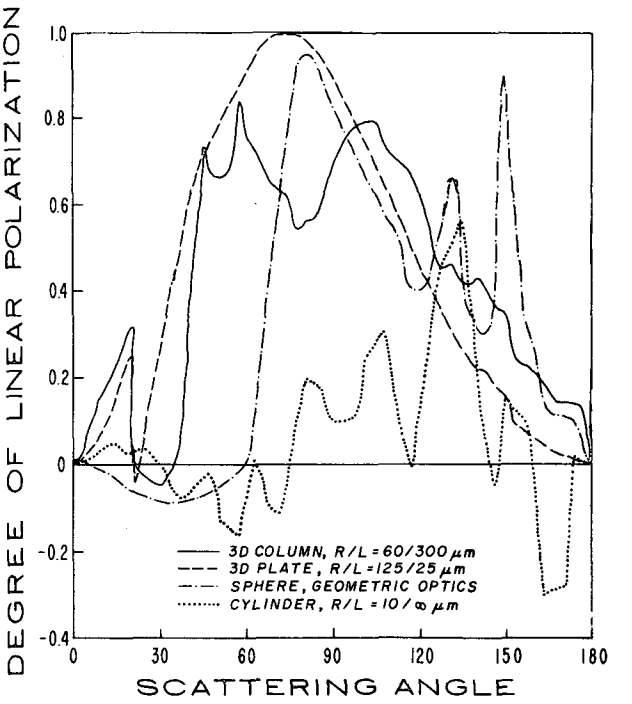

FIG. 9. Comparison of linear polarization for 3D plates and columns from the present study with linear polarization for spheres (Liou and Hansen, 1971) and 3D long circular cylinders (Liou, 1972).

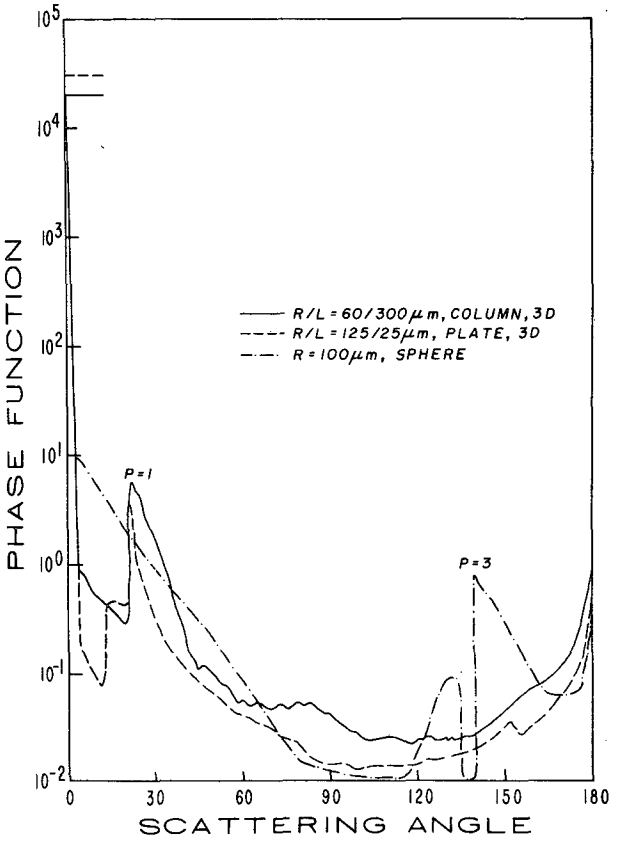

FIG. 8. Comparison of 3D phase functions for columns and plates from the present study with the phase function for spheres from Liou and Hansen (1971).

Fig. 11 shows the extinction and scattering cross sections and the single scattering albedo (see Section 2c) for large columns ($R/L = 60/300\ \mu m$) randomly oriented in a horizontal plane. The cross section units (on the left axis) are in μm^2. The albedo is scaled on the right axis from 0–0.8. The curves are plotted as functions of the elevation angle and the black triangles represent the value for randomly oriented columns in three-dimensional space. The solid curve is the extinction cross section σ_e for the aforementioned crystal size which is independent of the wavelength. Thus, this curve is the extinction cross section at any wavelength and it is also the scattering cross section for wavelengths where no adsorption takes place. The dotted line in the figure is the scattering cross section σ_s at the 10.6 μm wavelength. It is only slightly over half the value of σ_e at any elevation angle. The albedo $\tilde{\omega}_0$ is represented

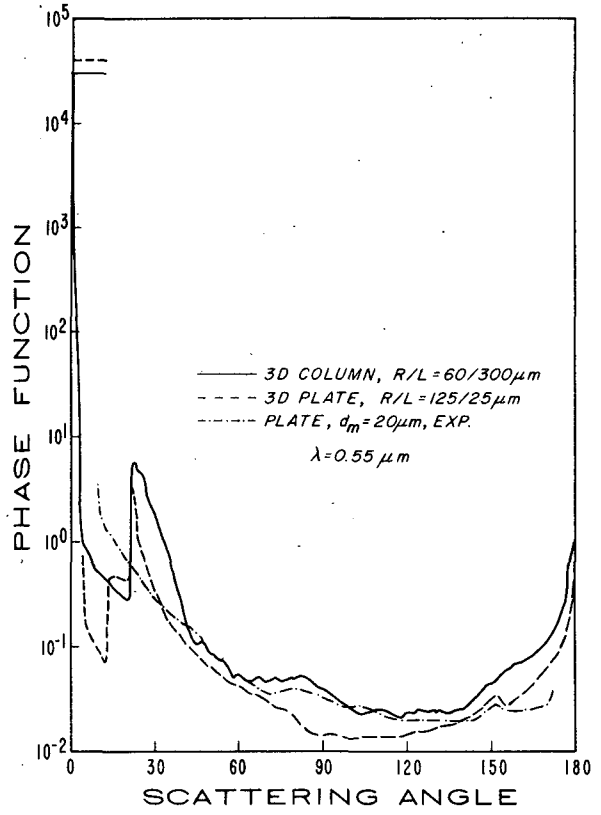

FIG. 10. Comparison of 3D phase functions for plates and columns from the present study with experimental data for small plates from Sassen and Liou (1979a).

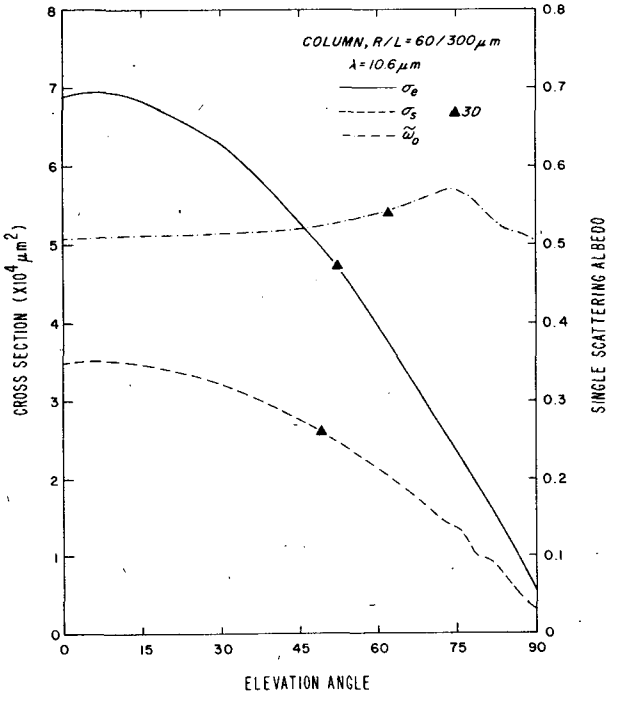

FIG. 11. Extinction and scattering cross sections for a column at the wavelength, $\lambda = 10.6\ \mu$m. The extinction (scattering) cross section is for all wavelengths without absorption.

by the dash-dot line. It is seen that the maximum value shown at 70° is just over 0.56 and that the absorption is never <45% of the incident light. For random orientation in three-dimensional space we find a value of 0.54 for the single scattering albedo at the 10.6 μm wavelength.

4. Discussion and concluding remarks

In the previous section we have provides some discussion of the physical origin of the common features for hexagonal crystals. As illustrated in Figs. 12c and 12d the 22 and 46° halos are minimum deviation paths for 60 and 90° prism angles, respectively. Since the general derivation for the minimum deviation angle for a given prism angle has been given in various sources, particularly Humphreys (1929), we shall not discuss this problem further in this study. However, in discussing the 8° halo and the peak near 153°, it should be pointed out that a smooth external reflection profile is responsible for the surrounding lower values.

The 8° halo, as noted previously, is basically produced by long thin columns. It is caused by oblique rays incident at an elevation angle near 60°. At this angle the effective index of refraction in the $X-Y$ plane m_r is about 2. With this index of refraction, light incident at $\phi \approx 86°$ is scattered near $\theta \approx 8°$ after two internal reflections (see Fig. 12a). The en-

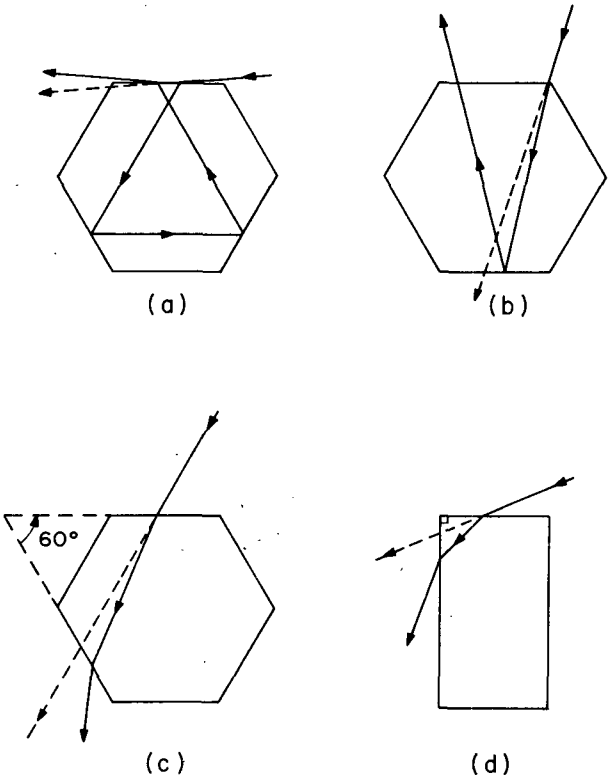

FIG. 12. Physical causes of selected features: (a) 8° halo; (b) feature near 153°; (c) 22° halo; (d) 46° halo.

ergy values corresponding for rays having angles $\phi > 87°$ are lower than those for the 8° halo since external reflection removes more energy from the beam. For cases involving $\phi < 85°$, the energy values also are lower since fewer rays can make the reflections necessary. Thus, the 8° halo is formed by two competing processes which reach an optimum near this angle.

As illustrated in Fig. 12b, the feature near 153° is caused by one internal reflection. The smooth surrounding profile in the phase function curves is generally given by external reflection. For rays incident normally on the hexagon having an azimuthal angle ϕ of $<40.95°$ (with $\theta = 0$), the reflection internally brings the rays back to the entry face at the same angle as external reflection. Again, two competing processes raise phase function values over the external profile near the 153° scattering angle. For rays having angles $\phi < 15°$, the external reflected energy is lower than the ray at $\phi = 16°$, while for $\phi > 17°$ cases the number of rays which can return to the entry face is much more reduced. These two processes reach their optimum near the 153° scattering angle.

We have seen from illustrations presented in Section 3 that scattering and polarization patterns for hexagons differ greatly from spheres and circular cylinders. In fact, the polarization signature for particles of circular versus hexagonal cross sections is distinctive enough, especially between 30 and 60° and between 130 and 140°, to allow easy differentiation between the two. More surprising is the variance between the linear polarization patterns for columns and plates. This leads us to believe that in thin ice clouds, where single scattering is dominant, plate-type ice crystals might be distinguished from column-type ice crysals utilizing the polarization information. Further research based on ray-tracing programs should include more intensive study of linear polarization from various shapes and sizes of ice crystals, as well as an attempt to solve the radiative transfer equation using the derived cross sections and phase functions for randomly oriented ice crystals both in two- and three-dimensional space.

Acknowledgments. This research was supported by the Division of Atmospheric Sciences of the National Science Foundation under Grant ATM78-26259 and in part by the Air Force Office of Scientific Research under Contract F49620-79-C-0198.

REFERENCES

Born, M., and E. Wolf, 1975: *Principles of Optics*, 5th ed. Pergamon Press, 808 pp.

Greenler, R. G., A. J. Mallman, J. R. Mueller and R. Romito, 1977: Form and origin of the parry arcs. *Science*, **195**, 360–367.

Humphreys, W. J., 1929: *Physics of Air*. McGraw-Hill, 654 pp.

Jacobowitz, H., 1971: A method for computing the transfer of solar radiation through clouds of hexagonal ice crystals. *J. Quant. Spectrosc. Radiat. Transfer*, **11**, 691–695.

Liou, K. N., 1972: Light scattering by ice clouds in the visible and infrared: A theoretical study. *J. Atmos. Sci.*, **29**, 524–536.

——, 1980: *An Introduction to Atmospheric Radiation*. Academic Press, 404 pp.

——, and J. E. Hansen, 1971: Intensity and polarization for single scattering by polydisperse spheres: A comparison of ray optics and Mie theory. *J. Atmos. Sci.*, **28**, 995–1004.

——, R. Baldwin and T. Kaser, 1976: Preliminary experiments on the scattering of polarized laser light by ice crystals. *J. Atmos. Sci.*, **33**, 553–557.

Sassen, K., and K. N. Liou, 1979a: Scattering of polarized laser light by water droplet, mixed phase, and ice crystal clouds. Part I: Angular scattering patterns. *J. Atmos. Sci.*, **36**, 838–850.

——, and ——, 1979b: Scattering of polarized laser light by water droplet, mixed phase, and ice crystal clouds. Part II: Angular depolarization and multiple-scattering behavior. *J. Atmos. Sci.*, **36**, 851–861.

Schwartz, M., 1972: *Principles of Electrodynamics*. McGraw-Hill, 342 pp.

Wendling, P., R. Wendling and H. K. Weickmann, 1979: Scattering of solar radiation by hexagonal ice crystals. *Appl. Opt.*, **18**, 2663–2671.